RSC Advances

ROYAL SOCIETY OF CHEMISTRY

PAPER

View Article Online
View Journal | View Issue

Check for updates

Cite this: *RSC Adv.*, 2023, **13**, 4150

Synthesis of $WO_3@WS_2$ core–shell nanostructures *via* solution-based sulfurization for improved performance of water splitting

Jianming Lai,[ab] Bingjie Wang,[a] Yuedong Gong,[a] Chenwei Sun,[a] Weilin Wang[c] and Weiguang Yang *[abd]

Received 9th October 2022
Accepted 28th November 2022

DOI: 10.1039/d2ra06354a

rsc.li/rsc-advances

High light absorption capacity and excellent charge transportation are significant for superior water-splitting performance. Here, WO_3/WS_2 core–shell nanowire arrays were fabricated using a two-step hydrothermal method. The crystal phase, morphology, crystal structure, chemical composition, and optical properties were characterized using XRD, SEM, TEM, XPS, and UV-vis spectroscopy. Consequently, the photocurrent density of the as-prepared WO_3/WS_2 photoanode was 0.91 mA cm^{-2} (at 1.23 V *vs.* RHE), which showed a 112% increase compared to that with pristine WO_3. The enhanced photoelectrochemical performance, we believe, was due to the promoted light response and improved separation as well as transportation at the WO_3/WS_2 interface.

1. Introduction

Compared with other hydrogen production techniques, photoelectrochemical (PEC) water splitting, which can directly convert solar energy into hydrogen, has emerged as a promising method to generate hydrogen due to its many advantages including sustainability and no pollutants.[1–4] In 1972, using TiO_2 as a photoanode in PEC water splitting was first reported by Fujishima and Honda.[5] Since then, a huge amount of semiconductors have been tried as photoelectrodes, particularly many metal oxides.[6–8]

Among various materials, tungsten trioxide (WO_3), with a band gap at around 2.8 eV, has intrigued a lot of interest due to the following advantages: non-toxicity, high resistance to photocorrosion, a moderate hole diffusion length (~150 nm), superior electron mobility (~12 $cm^2\ V^{-1}\ s^{-1}$) and a suitable valence band position for water oxidation.[9–12] However, the PEC performance of WO_3 is still not efficient enough due to two important problems: the recombination of photogenerated electron and hole pairs in the bulk, as well as a relative large band gap value.[13,14] Thus, coupling with a narrow band gap semiconductor to form a heterostructure, seems to be an effective strategy to boost the PEC performance of WO_3. For instance, Zheng reported a *Z*-scheme WO_3/Cu_2O heterojunction for enhanced PEC performance without external bias.[15] Many other heterostructures, including WO_3/Co_3O_4, $WO_3/BiVO_4$, WO_3/g-C_3N_4, WO_3/Ag_2S, and WO_3/Sb_2S_3 have also exhibited excellent PEC performance, which is due to more charge separation and transportation at the interface.[13,16–21] Nevertheless, most of these studies have to consider the problem of lattice matching at the interface, which might induce some defects.

In particular, WO_3/WS_2 *Z*-scheme heterostructures have recently attracted considerable attention because of their unique structure. WS_2 is an indirect band gap semiconductor with a good PEC activity,[22] which matches well with WO_3.[23] Seo *et al.* reported an approach for synthesizing WO_3/WS_2 core–shell structures utilizing the $WO_3\cdot0.33H_2O$ phase using H_2S gas for sulfurization.[24] Lee *et al.* synthesized edge-exposed 1T phase WS_2 on WO_3 nanohelixes arrays by pre-annealing and CVD.[25]

Our approach was to create a sulfurized shell by a simple hydrothermal sulfurization process, which is more facile than others. Depending on this method, a WS_2 shell was successfully synthesized at the surface of WO_3 with intimate contact.

In this work, vertically-aligned one-dimensional (1-D) WO_3 nanowire arrays were synthesized on the FTO substrate using the hydrothermal method. Then, after a simple sulfurization process, a narrow band gap WS_2 was coated on the surface of WO_3. The obtained photocurrent density of WO_3/WS_2 core–shell nanowire arrays increased by 112% compared to that of pristine WO_3 nanowires. The enhanced PEC performance was illustrated through the investigation of crystal structure, morphology characterization, and optical properties. Furthermore, the application of a simple sulfurization process was helpful for the construction of visible-light active photoanode with high stability under illumination.

---

[a] *Department of Electronic Information Materials, School of Materials Science and Engineering, Shanghai University, Shanghai 200444, China*
[b] *Zhejiang Institute of Advanced Materials, SHU, Jiashan, 314113, China*
[c] *Henan Power Battery Innovation Center Co., Ltd, No. 416, Muye Avenue, Xinxiang, 453004, China*
[d] *Collaborative Innovation Center of Henan Province for Motive Power and Key Materials, College of Chemistry and Chemical Engineering, Henan Normal University, Xinxiang, 453007, China*

2. Experimental section

2.1 The growth of WO_3 nanowire arrays

WO_3 nanowire arrays were synthesized on an FTO substrate using the hydrothermal method. First of all, a dense layer was spin-coated on a cleaned FTO substrate followed by annealing at 500 °C using a solution containing 10 mL, 0.7 g titanium tetraisopropanolate (TTIP), and 12 μL of 36% HCL. Separately, 8.3 g of $Na_2WO_4 \cdot 2H_2O$ was dissolved in 25 mL deionized water (DIW) and then a mixed acid solution (the mole ratio of HCl and H_2SO_4 was 5 : 1) was slowly added until the pH value of the solution was approximately 3.2–3.5. Then, the pH value of this solution was adjusted to 4.2 using DIW. Forth, 1.0 g oxalic acid was added to adjust the pH value to about 1.9. Finally, the FTO substrate with a compact TiO_2 dense layer was immersed in a sealed Teflon-lined stainless-steel autoclave filled with the above precursor solution with 0.5 g of Rb_2SO_4. The hydrothermal reaction was performed at 180 °C for 15 h.

2.2 Constructing WO_3/WS_2 core–shell heterostructure

A WS_2 shell was coated by sulfurizing the surface of WO_3 nanowires by a second hydrothermal step at 180 °C with a varied growth time for 5 h, 10 h, and 15 h. The WO_3 nanowire arrays were placed in a sealed Teflon-lined stainless-steel autoclave containing 15 mL 0.1 M thioacetamide. After the sulfurization reaction, the samples were washed with DIW, as well as with ethanol, and then dried in the air.

2.3 Characterization

X-ray diffraction (XRD) patterns were collected using a Rigaku D/max-2200 V diffractometer with Cu Kα radiation. The morphology of the samples was studied by field-emission scanning electron microscopy (FESEM) on a M-6700F (JEOL) microscope. X-ray photoelectron spectroscopy (XPS) analysis was carried out on an ESCA-Lab 250Xi X-ray photoelectron spectrometer. The transmission electron microscopy (TEM) measurements were performed on a JEM-2010F (JOEL) microscope. The ultraviolet-visible (UV-vis) absorption spectra were collected on a TU-1901 UV-vis absorption spectrophotometer (PERSEE, China).

2.4 PEC measurements

The relative PEC performances were studied on a photoelectrochemical working station (CHI660E) using a typical three electrodes system in 1 M NaOH (pH ≈ 13.6). The WO_3/WS_2 core–shell nanowires worked as a working electrode, Pt sheet as the counter electrode, and a saturated calomel electrode (SCE) as the reference electrode. The SCE was transferred into RHE using the following equation: $E_{\mathrm{RHE}} = E_{\mathrm{SCE}} + 0.241\ \mathrm{V} + 0.059 \times \mathrm{pH}$. The samples were illuminated with a solar light simulator (Newport) connected with AM 1.5 G filter. The linear sweep voltammetry (LSV) potential was scanned from −1.5 to 1.5 V at a rate of 50 mV S^{-1}. Chronoamperometry curves were collected at 0.185 V (*vs.* SCE) in 1800 seconds.

3. Results and discussion

3.1 Crystal structure, surface information, and chemical composition

XRD patterns (Fig. 1a) of the WO_3 and WO_3/WS_2 nanowire provided insight into the crystal structure obtained from the hydrothermal method. The pristine WO_3 gave three diffraction peaks at 13.98°, 23.38°, and 33.64°, which corresponded to (100), (002), and (112) crystal facets, respectively, (JCPDS No. 85-2460). Furthermore, the intensity of the (002) facet was strongest, indicating that the WO_3 nanowire with (002) preferential growth orientation was consistent with the *c*-axis of the nanowire. Similar XRD patterns were reported for WO_3 nanowires.[26,27] After sulfurization, the formation of a new diffraction peak could be observed at 14.3°, corresponding to the (002) crystal face of WS_2 (JCPDS No. 08-0237). To reveal the morphological change of the nanowire arrays, the morphology of WO_3 and WO_3/WS_2 nanowire arrays was characterized by FESEM. Fig. 1b exhibits the top-view SEM images of pure WO_3

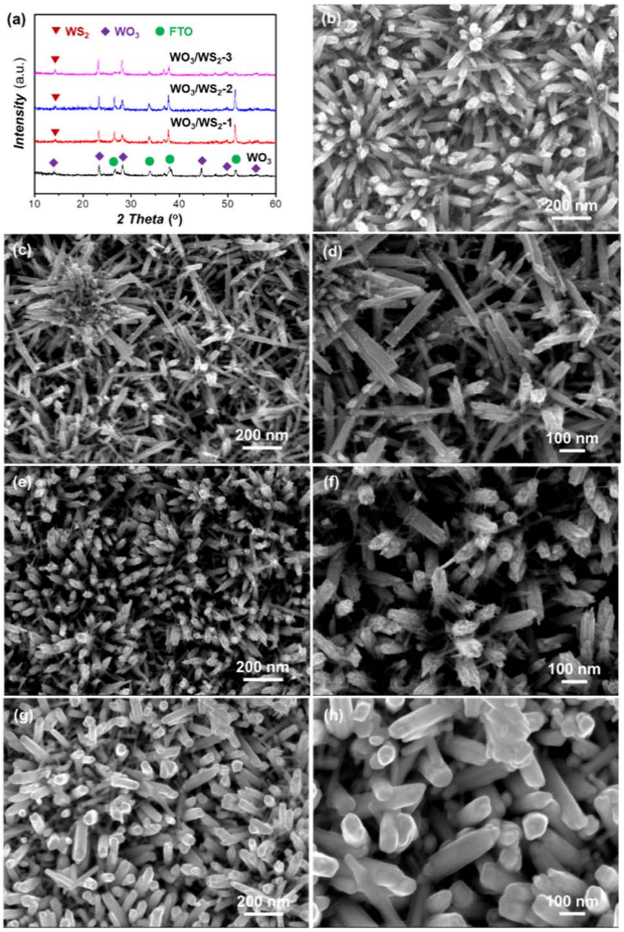

Fig. 1 (a) XRD patterns of pristine and sulfurized WO_3 nanowire arrays. (b) Top view SEM images of WO_3 nanowire arrays grown at 180 °C for 15 h (c, e and g). Top view SEM images of WO_3/WS_2 nanowire arrays synthesized at 180 °C for 5 h, 10 h and 15 h (d, f and h). High-resolution SEM images of WO_3/WS_2 nanowire arrays synthesized at 180 °C for 5 h, 10 h and 15 h.

synthesized at 180 °C for 15 h. WO_3 nanowire arrays were grown uniformly on the FTO substrate and the average diameter of the nanowire was about 72 nm. We treated the WO_3 nanowire arrays by sulfurization process at 180 °C for 5 h, 10 h, and 15 h, aiming to encapsulate WS_2 on the surface of nanowires, as shown in Fig. 1c–h. Fig. 1c, e, and g display the top-view SEM images of different samples grown at 5 h, 10 h, and 15 h, respectively. Fig. 1d, f, and h are the corresponding high-resolution SEM images. The nanowires of WO_3/WS_2 at 5 h were rough and independent. Along with the reaction time, it is obvious to find that the diameter of the nanowire became thicker and the surface became smooth. This change indicates the successful coating of the surface WS_2, which is consistent with the XRD results.

In order to obtain the microcrystal structure and surface information of WO_3/WS_2 core–shell nanowire arrays, the TEM measurements were carried out. As shown in Fig. 2a, which exhibits a low-magnification TEM image of WO_3/WS_2 core–shell nanowire arrays, a clear regular shape could be observed. In Fig. 2b and c, a clear interface between the core WO_3 and shell WS_2 could be observed from the high-resolution transmission electron microscopy (HRTEM) images, revealing the intimate combination of the core/shell structure. The WS_2 shell thickness was measured to be 13 nm. Fig. 2c shows an interplanar distance of 0.38 nm, which is consistent with the (002) crystal plane distance of WO_3. The interplanar distance of the shell was measured to be 0.15 nm, which matches well with the (008) plane of WS_2. This good lattice match between the core and shell is beneficial to decrease the combination possibility in the bulk and promote the charge transport between the WO_3 and WS_2 interface.

To further survey the elements distribution of the WO_3/WS_2 core–shell structure, an individual nanowire was characterized by HRTEM coupled with energy dispersive X-ray spectroscopy (EDS). Fig. 3a shows the HRTEM image of a single nanowire and Fig. 3b–d shows the corresponding elemental map of O, S, and W. It is obvious that W and O elements have higher signals, also indicating relative uniform distribution across the nanowire. The presence of the signal of the S element further confirms the formation of the WO_3/WS_2 core–shell structure.

In order to explicate the chemical composition of the nanowire arrays, XPS measurements were performed. Fig. 4 displays the high-resolution XPS spectra of W and S elements. As seen in Fig. 4a, the binding energy of the W $4f_{7/2}$ and W $4f_{5/2}$ appear at 35.7 eV and 37.8 eV, which are consistent with the values of bare WO_3 from the relevant literature.[17,28,29] The differentiation between W $4f_{7/2}$ and W $4f_{5/2}$ was about 2.1 eV, indicating the typical binding energy of W^{6+}. Nevertheless, there is a shift in the binding energy of W 4f after sulfurization. The peaks for W $4f_{7/2}$ and W $4f_{5/2}$ were observed at 32.58 eV and 35.58 eV, respectively, suggesting the existence of the tetravalent tungsten.[23] Fig. 4b shows the XPS results of S 2p, the signal of S 2p could not be found in pure WO_3. However, the peak of S 2p was observed after sulfurization. The fine spectrum of S 2p in the sulfurized WO_3 showed two different peaks at 162.21 eV and 163.28 eV, which are attributed to the S $2p_{3/2}$ and S $2p_{1/2}$, respectively, of S–W in WS_2.[22,30] Combining the aforementioned results, we could acknowledge the successful synthesis of WO_3/WS_2 core–shell structure.

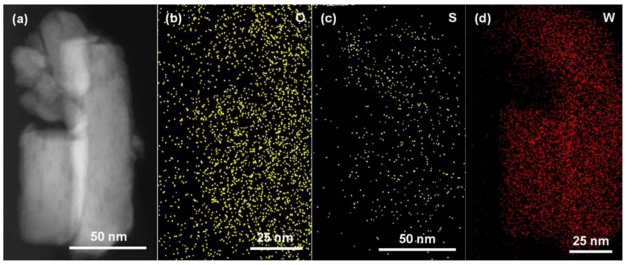

Fig. 3 (a) HRTEM image of WO_3/WS_2 core–shell nanowire prepared at 180 °C for 15 h. (b–d) EDS of the selected area.

3.2 Photoelectrochemical properties of the WO_3/WS_2 core–shell structure photoanode

The optical properties of WO_3 and WO_3/WS_2 core–shell nanowire arrays were characterized using UV-vis. As depicted in Fig. 5a, the pure WO_3 has an absorption edge at 445 nm. Compared with pristine WO_3, a red shift was observed in the WO_3/WS_2 samples, which is due to the formation of a narrow band gap WS_2 on the surface of WO_3. According to the Kubelka–Munk equation, the band gap of a semiconductor could be calculated:

$$\alpha h\nu = A(h\nu - E_g)^{n/2}$$

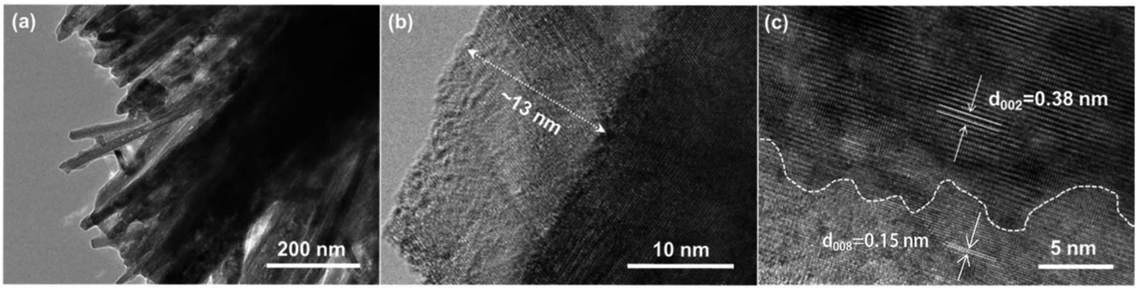

Fig. 2 Structural characterization of the WO_3-based nanowire arrays. (a) TEM image of the WO_3/WS_2 nanowire arrays. (b and c) HRTEM images of individual WO_3/WS_2 core–shell nanowire.

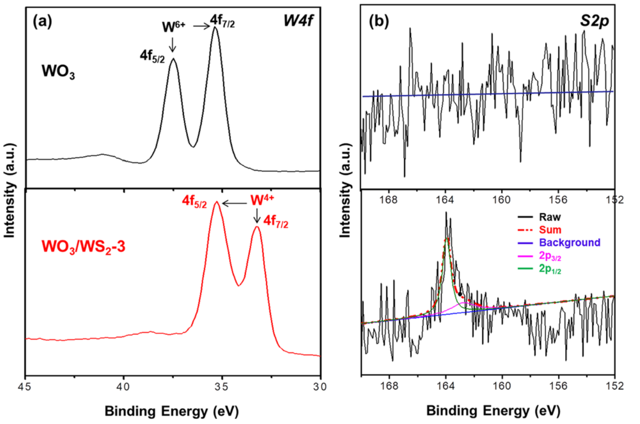

Fig. 4 High resolution XPS spectra of (a) W 4f peak and (b) S 2p peak of the samples. Top: pure WO_3; bottom: WO_3/WS_2 core–shell nanowire.

where α represents the absorption, h is the Planck constant, ν on behalf of the light frequency, A is the proportionality and E_g is the energy band gap. The value of n for a direct band gap semiconductor is 1, while n is 4 for the indirect band gap semiconductor. Therefore, the band gap value of bare WO_3 was calculated to be 2.78 eV, whereas the E_g values of WO_3/WS_2 grown at 5 h, 10 h, and 15 h were 2.70 eV, 2.65 eV, and 2.57 eV, respectively. As shown in Fig. 5b, the band gap of the sulfurized samples is narrower than that of pure WO_3, which is consistent with the promoted light absorption ability.

The photoelectrochemical (PEC) properties of WO_3 and WO_3/WS_2 nanowires were evaluated by measuring the photocurrent density at 1.23 V (*vs.* revisable hydrogen electrode, RHE) in 1 M NaOH solution. As shown in Fig. 6a, the photocurrent density (J_{ph}) of the bare WO_3 nanowire was 0.43 mA cm^{-2} (at 1.23 V *vs.* RHE). After sulfurization, the WO_3/WS_2 nanowire prepared at 180 °C for 15 h showed the highest J_{ph} (0.91 mA cm^{-2}), increased by 112% compared with bare WO_3. The J_{ph} of WO_3/WS_2 nanowires fabricated at 180 °C for 5 h and 10 h were 0.58 mA cm^{-2} and 0.81 mA cm^{-2}, respectively, which is still larger than that of pure WO_3. The large increase in the photocurrent density shows that the core–shell structure greatly improves the PEC properties of WO_3. The enhanced light absorption of the WS_2 shell, as proved in Fig. 5, could be one of the reasons, but cannot fully explain such a large increase in performance. In the next section, we analyzed its energy band mechanism to explain this phenomenon.

Apart from the excellent PEC performance, the stability of the photoanode is very crucial for practical applications. The chronoamperometry measurements were performed to investigate the stability of WO_3 and WO_3/WS_2 nanowire arrays. As seen in Fig. 6b, the J_{ph} of all samples remained the same during the entire experiment and showed no degradation tendency, suggesting that WO_3/WS_2 nanowiress have good stability as well as an anti-photo corrosion ability. Furthermore, the samples exhibited a quick photoresponse during the light chopping, which meant a more efficient charge separation and transportation at the WO_3/WS_2 interface due to the construction of the heterostructure.

3.3 Photocatalytic mechanism of the WO_3/WS_2 core–shell structure photoanode

Seo *et al.*[24] and Lee *et al.*[25] reported WO_3/WS_2 nanowires structured *Z*-scheme heterojunction, and the schematic diagram of the energy band structure as shown in Fig. 7. As the shell of the thickness of WS_2 was approximately 13 nm, both WO_3 and WS_2 could be excited. Excited electrons and holes are generated in the conduction and valence bands of WO_3 and WS_2, respectively. Since the VBM of WS_2 is higher than that of WO_3, the electrons flowed from WS_2 to WO_3 spontaneously.[7] Similarly, holes spontaneously flowed from WO_3 to WS_2. Therefore, positive and negative charges are concentrated on the WS_2 and WO_3 surfaces. Then, the electrons were transferred to a counter electrode *via* the back contact, and an external circuit was used in the reduction reactions. As a result, the heterojunction of WO_3/WS_2 not only efficiently separated the photogenerated electron–hole pairs but also effectively transported electrons and holes into the cathode and anode for the hydrogen- and oxygen-evolution reactions, respectively.

The PEC water splitting performance was governed by many factors, including the phase structure, light absorption ability,

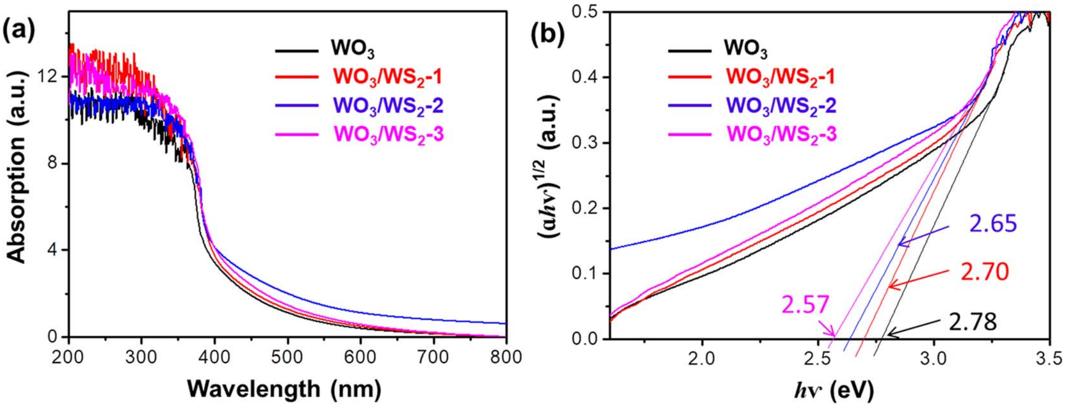

Fig. 5 (a) UV-vis spectra and (b) plots of the $(\alpha h\nu)^{1/2}$ *vs.* photon energy ($h\nu$) of WO_3 and WO_3/WS_2 core–shell nanowire arrays synthesized at 180 °C for 5 h, 10 h and 15 h (WO_3/WS_2-1, 2 and 3).

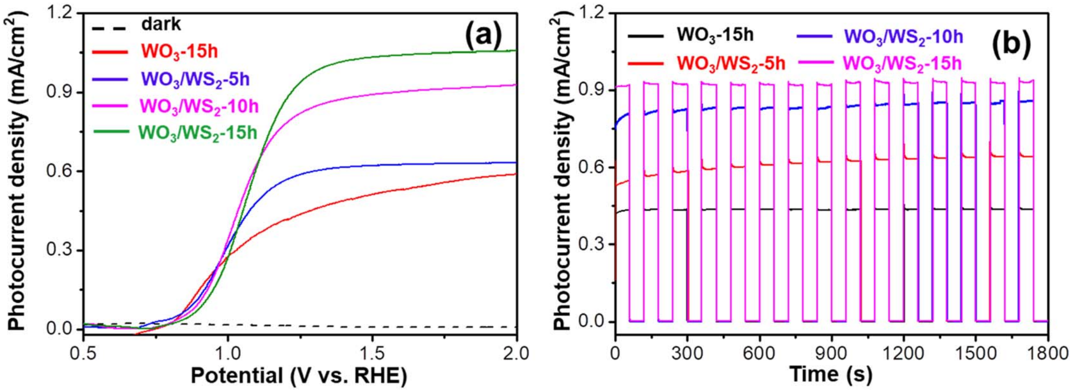

Fig. 6 Photoelectrochemical measurements of pristine WO_3 and WO_3/WS_2 core–shell nanowire arrays synthesized at 180 °C for 5 h, 10 h and 15 h (a) photocurrent density–potential (J_{ph}–V) curves and (b) chronoamperometry plots in 1800 s. Measured in 1 M NaOH under AM 1.5 G illumination.

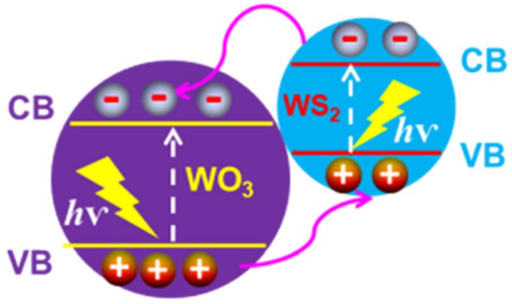

Fig. 7 Schematic illustration of the energy band alignment of $WO_3@WS_2$ core–shell for photoelectrochemical water splitting.

separation and transportation efficiency of photoexcited charges, and stability. Combining the XRD and SEM results, the synthesized nanowire arrays show good crystallinity. The TEM and XPS results confirmed the good contact between the WS_2 shell and WO_3 core, which facilitated the charge transportation. The shell WS_2 with a narrower band gap, as demonstrated in Fig. 5, enhanced the light absorption.

Therefore, it can be concluded that the WO_3/WS_2 core–shell formed a heterostructure, which not only boosted the light response but also accelerated the separation as well as the transportation of photogenerated charges for efficient PEC water splitting.

4. Conclusion

In summary, uniform WO_3/WS_2 core–shell nanowire arrays were synthesized by a simple hydrothermal method. The highest photocurrent density of the WO_3/WS_2 (15 h) nanowire was 0.91 mA cm^{-2} (at 1.23 V *vs.* RHE), while pure WO_3 only reached 0.43 mA cm^{-2}. Besides, all the samples showed excellent stability under illumination. The enhanced photoelectrochemical performance was due to the formation of a WS_2 shell on the surface of WO_3, which enhances light absorption ability as well as the charge separation and transportation of the photoanode. The successful synthesis of WO_3/WS_2 core–shell nanowires by sulfurization paves a new path for the design of narrow-band gap water-splitting materials with high stability.

Conflicts of interest

There are no conflicts to declare.

Acknowledgements

This work is supported by Henan Power Battery Innovation Center Co., Ltd and the Science and Technology Commission of Shanghai (No. 17010500600).

References

1 M. Gratzel, Photoelectrochemical cells, *Nature*, 2001, **414**, 338–344.
2 C. Jiang, S. J. A. Moniz, A. Wang, T. Zhang and J. Tang, Photoelectrochemical devices for solar water splitting – materials and challenges, *Chem. Soc. Rev.*, 2017, **46**, 4645–4660.
3 P. Lianos, Review of recent trends in photoelectrocatalytic conversion of solar energy to electricity and hydrogen, *Appl. Catal., B*, 2017, **210**, 235–254.
4 M. G. Walter, E. L. Warren, J. R. McKone, S. W. Boettcher, Q. X. Mi, E. A. Santori and N. S. Lewis, Solar Water Splitting Cells, *Chem. Rev.*, 2010, **110**, 6446–6473.
5 A. Fujishima and K. Honda, Electrochemical photolysis of water at a semiconductor electrode, *Nature*, 1972, **238**, 37–38.
6 F. E. Osterloh, Inorganic materials as catalysts for photochemical splitting of water, *Chem. Mater.*, 2008, **20**, 35–54.
7 T. Hisatomi, J. Kubota and K. Domen, Recent advances in semiconductors for photocatalytic and photoelectrochemical water splitting, *Chem. Soc. Rev.*, 2014, **43**, 7520–7535.
8 K. Sivula and R. van de Krol, Semiconducting materials for photoelectrochemical energy conversion, *Nat. Rev. Mater.*, 2016, **1**, 15010.

9 P. Dias, T. Lopes, L. Meda, L. Andrade and A. Mendes, Photoelectrochemical water splitting using WO3 photoanodes: the substrate and temperature roles, *Phys. Chem. Chem. Phys.*, 2016, **18**, 5232–5243.

10 G. Zheng, J. Wang, H. Liu, V. Murugadoss, G. Zu, H. Che, C. Lai, H. Li, T. Ding, Q. Gao and Z. Guo, Tungsten oxide nanostructures and nanocomposites for photoelectrochemical water splitting, *Nanoscale*, 2019, **11**, 18968–18994.

11 Y. Wang, W. Tian, C. Chen, W. Xu and L. Li, Tungsten Trioxide Nanostructures for Photoelectrochemical Water Splitting: Material Engineering and Charge Carrier Dynamic Manipulation, *Adv. Funct. Mater.*, 2019, **29**, 1809036.

12 S. S. Kalanur, Y. J. Hwang, S. Y. Chae and O. S. Joo, Facile growth of aligned WO3 nanorods on FTO substrate for enhanced photoanodic water oxidation activity, *J. Mater. Chem. A*, 2013, **1**, 3479–3488.

13 J. Zhang, Z. Liu and Z. Liu, Novel WO_3/Sb_2S_3 Heterojunction Photocatalyst Based on WO_3 of Different Morphologies for Enhanced Efficiency in Photoelectrochemical Water Splitting, *ACS Appl. Mater. Interfaces*, 2016, **8**, 9684–9691.

14 S. Wang, H. Chen, G. Gao, T. Butburee, M. Lyu, S. Thaweesak, J.-H. Yun, A. Du, G. Liu and L. Wang, Synergistic crystal facet engineering and structural control of WO_3 films exhibiting unprecedented photoelectrochemical performance, *Nano Energy*, 2016, **24**, 94–102.

15 G. Zheng, J. Wang, H. Li, Y. Li and P. Hu, WO_3/Cu_2O heterojunction for the efficient photoelectrochemical property without external bias, *Appl. Catal., B*, 2020, **265**, 118561.

16 S. Zhang, J. Wang, S. Chen, R. Li and T. Peng, Construction of Ag2S/WO3 Direct *Z*-Scheme Photocatalyst for Enhanced Charge Separation Efficiency and H_2 Generation Activity, *Ind. Eng. Chem. Res.*, 2019, **58**, 14802–14813.

17 L. Huang, H. Xu, Y. Li, H. Li, X. Cheng, J. Xia, Y. Xu and G. Cai, Visible-light-induced WO_3/g-C_3N_4 composites with enhanced photocatalytic activity, *Dalton Trans.*, 2013, **42**, 8606–8616.

18 J. Su, L. Guo, N. Bao and C. A. Grimes, Nanostructured $WO_3/BiVO_4$ Heterojunction Films for Efficient Photoelectrochemical Water Splitting, *Nano Lett.*, 2011, **11**, 1928–1933.

19 B. R. Lee, M. G. Lee, H. Park, T. H. Lee, S. A. Lee, S. S. M. Bhat, C. Kim, S. Lee and H. W. Jang, All-Solution-Processed $WO_3/BiVO_4$ Core–Shell Nanorod Arrays for Highly Stable Photoanodes, *ACS Appl. Mater. Interfaces*, 2019, **11**, 20004–20012.

20 F. Zhan, J. Li, W. Li, Y. Liu, R. Xie, Y. Yang, Y. Li and Q. Chen, *In situ* formation of $CuWO_4/WO_3$ heterojunction plates array films with enhanced photoelectrochemical properties, *Int. J. Hydrogen Energy*, 2015, **40**, 6512–6520.

21 A. A. Markhabayeva, M. Moniruddin, R. Dupre, K. A. Abdullin and N. Nuraje, Designing of $WO_3@Co_3O_4$ Heterostructures to Enhance Photoelectrochemical Performances, *J. Phys. Chem. A*, 2020, **124**, 486–491.

22 M. S. Akple, J. Low, S. Wageh, A. A. Al-Ghamdi, J. Yu and J. Zhang, Enhanced visible light photocatalytic H_2-production of g-C_3N_4/WS_2 composite heterostructures, *Appl. Surf. Sci.*, 2015, **358**, 196–203.

23 X. Wang, G. Hai, B. Li, Q. Luan, W. Dong and G. Wang, Construction of dual-*Z*-scheme WS_2-$WO3\cdot H_2O$/g-C_3N_4 catalyst for photocatalytic H_2 evolution under visible light, *Chem. Eng. J.*, 2021, **426**, 130822.

24 D.-B. Seo, S. Yoo, V. Dongquoc, T. N. Trung and E.-T. Kim, Facile synthesis and efficient photoelectrochemical reaction of WO_3/WS_2 core@shell nanorods utilizing $WO_3\cdot 0.33H_2O$ phase, *J. Alloys Compd.*, 2021, **888**, 161587.

25 N. Lee, I. Y. Choi, K.-Y. Doh, J. Kim, H. Sim, D. Lee, S.-Y. Choi and J. K. Kim, Enhanced catalytic activity of edge-exposed 1T phase WS_2 grown directly on a WO_3 nanohelical array for water splitting, *J. Mater. Chem. A*, 2019, **7**, 26378–26384.

26 J. Zhang, J.-p. Tu, X.-h. Xia, X.-l. Wang and C.-d. Gu, Hydrothermally synthesized WO_3 nanowire arrays with highly improved electrochromic performance, *J. Mater. Chem.*, 2011, **21**, 5492–5498.

27 P. M. Rao, L. Cai, C. Liu, I. S. Cho, C. H. Lee, J. M. Weisse, P. Yang and X. Zheng, Simultaneously Efficient Light Absorption and Charge Separation in $WO_3/BiVO_4$ Core/Shell Nanowire Photoanode for Photoelectrochemical Water Oxidation, *Nano Lett.*, 2014, **14**, 1099–1105.

28 G. Lu, X. Li, Z. Qu, Q. Zhao, H. Li, Y. Shen and G. Chen, Correlations of WO_3 species and structure with the catalytic performance of the selective oxidation of cyclopentene to glutaraldehyde on WO_3/TiO_2 catalysts, *Chem. Eng. J.*, 2010, **159**, 242–246.

29 L. Jiang, X. Yuan, G. Zeng, J. Liang, X. Chen, H. Yu, H. Wang, Z. Wu, J. Zhang and T. Xiong, In-situ synthesis of direct solid-state dual *Z*-scheme WO_3/g-C_3N_4/Bi_2O_3 photocatalyst for the degradation of refractory pollutant, *Appl. Catal., B*, 2018, **227**, 376–385.

30 D. Lin, Y. Zhou, X. Ye and M. Zhu, Construction of sandwich structured photocatalyst using monolayer WS_2 embedded g-C_3N_4 for highly efficient H_2 production, *Ceram. Int.*, 2020, **46**, 12933–12941.